




# Absolute quantification of tumor-infiltrating immune cells in high-grade glioma identifies prognostic and radiomics values

A. Reum Kim<sup>1</sup> · Kyu Sung Choi<sup>1</sup> · Min-Sung Kim<sup>2,3</sup> · Kyung-Min Kim<sup>2,3</sup> · Ho Kang<sup>2,3</sup> · Sojin Kim<sup>2,3</sup> · Tamrin Chowdhury<sup>2,3</sup> · Hyeon Jong Yu<sup>2,3</sup> · Chae Eun Lee<sup>2,3</sup> · Joo Ho Lee<sup>3,4</sup> · Soon-Tae Lee<sup>3,5</sup> · Jae Kyung Won<sup>3,6</sup> · Jin Wook Kim<sup>2,3</sup> · Yong-Hwy Kim<sup>2,3</sup> · Tae Min Kim<sup>3,7</sup> · Sung-Hye Park<sup>3,6</sup> · Seung Hong Choi<sup>3,8</sup> · Eui-Cheol Shin<sup>1</sup> · Chul-Kee Park<sup>2,3</sup> 

Received: 3 October 2020 / Accepted: 17 December 2020 / Published online: 8 January 2021  
© The Author(s), under exclusive licence to Springer-Verlag GmbH, DE part of Springer Nature 2021

## Abstract

**Purpose** To understand the tumor immune microenvironment precisely, it is important to secure the quantified data of tumor-infiltrating immune cells, since the immune cells are true working unit. We analyzed unit immune cell number per unit volume of core tumor tissue of high-grade gliomas (HGG) to correlate their immune microenvironment characteristics with clinical prognosis and radiomic signatures.

**Methods** The number of tumor-infiltrating immune cells from 64 HGG core tissue were analyzed using flow cytometry and standardized. After sorting out patient groups according to diverse immune characteristics, the groups were tested if they have any clinical prognostic relevance and specific radiomic signature relationships. Sparse partial least square with discriminant analysis using multimodal magnetic resonance images was employed for all radiomic classifications.

**Results** The median number of CD45 + cells per one gram of HGG core tissue counted 865,770 cells which was equivalent to 8.0% of total cells including tumor cells. There was heterogeneity in the distribution of immune cell subpopulations among patients. Overall survival was significantly better in T cell-deficient group than T cell-enriched group ( $p=0.019$ ), and T8 dominant group than T4 dominant group ( $p=0.023$ ). The number of tumor-associated macrophages (TAM) and M2-TAM was significantly decreased in isocitrate dehydrogenase mutated HGG. Radiomic signature classification showed good performance in predicting immune phenotypes especially with features extracted from apparent diffusion coefficient maps.

**Conclusions** Absolute quantification of tumor-infiltrating immune cells confirmed the heterogeneity of immune microenvironment in HGG which harbors prognostic impact. This immune microenvironment could be predicted by radiomic signatures non-invasively.

**Keywords** Quantification · Tumor-infiltrating lymphocyte · Tumor-associated macrophage · High-grade glioma · Radiomics

---

A. Reum Kim, Kyu Sung Choi and Min-Sung Kim contributed equally to this work.

---

**Supplementary Information** The online version contains supplementary material available at <https://doi.org/10.1007/s00262-020-02836-w>.

- 
- ✉ Seung Hong Choi  
verocay@snuh.org
  - ✉ Eui-Cheol Shin  
ecshin@kaist.ac.kr
  - ✉ Chul-Kee Park  
nsckpark@snu.ac.kr

Extended author information available on the last page of the article

## Introduction

High-grade gliomas (HGGs) are undisputedly poorly prognostic central nervous system (CNS) tumors, and most patients die of the disease notwithstanding the current best management protocols. Tremendous strides have been made recently in the field of cancer immunotherapy, with relatively disappointing news for HGGs so far. Although the CNS is generally accepted as an immunologically privileged site, it has long been recognized that clinically relevant lymphocyte infiltration occurs in gliomas [1]. Recent anatomical discoveries in CNS lymphatics highly suggest active participation of immune cells in the brain tumor microenvironment [2, 3].

Empirically, diverse populations of immune cells have been found to exist intrinsically in glioma tissue [4–9]. However, there have been perennial debates on the prognostic impact and dominance of immune cell subpopulations in glioma [5, 10–16]. The inconsistent results are largely due to qualitative or semiquantitative analyses of immune cell phenotypes from unspecified tumor areas using diverse evaluation methodologies. Employing the expression level of surface markers in defining the immunophenotype of tumors using genomic data also connotes issues about the cross-reactivity of non-immune cell populations. Considering the nature of cancer immunobiology, precise assessments of the status of the tumor immune microenvironment should be based on the number of immune cells involved as a unit of analysis rather than the expression level of immune surface markers. Therefore, it is important to gain insights into the census figures of the immune microenvironment of the tumor tissue to understand their exact clinical relevance.

Recent advances in radiogenomics have shown that utilizing multimodal magnetic resonance imaging (MRI) to reflect the cellularity and perfusion characteristics of tumors enables a more accurate prediction of the status of genetic mutations [17, 18], which may lead to different immune phenotypes [12]. Because certain statuses of tumor immune microenvironments have been known to guide the tumor response to immunotherapy [19], multimodal MRI-based signatures that identify the immune phenotype can play a role as a potential biomarker for screening patients for immunotherapy and for the noninvasive monitoring of treatment responses as well as immune-related adverse events.

Here, we analyzed the unit immune cell number per unit volume of core tumor tissue to correlate the characteristics of the immune microenvironment and the clinical prognosis of HGG. Moreover, we also investigated whether multimodal MRI radiomics analysis can identify imaging-based biomarkers that can predict the immune phenotype.

## Materials and methods

### Patient samples

Fresh tumor tissues were obtained from 64 patients undergoing surgical resection of newly diagnosed HGG with informed consent in accordance with the approval of the institutional review board of Seoul National University Hospital (IRB No. H-1902-062-1010). Histological diagnosis revealed of 46 glioblastomas (GBM), 9 anaplastic oligodendrogliomas (AO), and 9 anaplastic astrocytomas (AA). Tissue specimens were collected from the core area of the tumor showing strong red intensity on 5-aminolevulinic acid fluorescence excluding the necrotic area and immersed in RPMI media at room temperature immediately

after surgical resection. After the tissue specimens were weighted, a MACS brain tumor dissociation kit (Miltenyi Biotec, Auburn, CA, USA) and gentleMACS™ Dissociators (Miltenyi Biotec, Auburn, CA, USA) were used to dissociate tissue samples within 2 h of collection, and debris was removed using MACS Debris Removal Solution (Miltenyi Biotec, Auburn, CA, USA) according to the manufacturer's protocol. Only samples with viable single cells that showed cell viability > 80% after dissociation were included in this study. Meanwhile, we found that the MACS brain tumor dissociation kit included an enzyme, papaya proteinase I, which mildly destroys cell surface epitopes, resulting in the downregulation of CD8 on the cell surface. However, we confirmed that the relative frequency of CD8<sup>+</sup> T cells was maintained even after using the MACS brain tumor dissociation kit.

### Antibodies

Multicolor flow cytometry was performed using the following fluorochrome-conjugated mAbs: anti-CD25-Brilliant Violet (BV) 421 (562442; clone M-A251), anti-CD19-BV605 (562653; clone SJ25C1), anti-CD4-BV650 (563875; clone SK3), anti-CD14-BV711 (563372; clone M $\phi$ P9), anti-CD3-BV786 (565491; clone UCTH1), anti-CD11c-Brilliant Blue 515 (564490; clone B-ly6), anti-CD45-PerCP-Cy5.5 (564105; clone HI30), anti-CD68-PE-CF594 (564944; clone Y1/82A), anti-CD163-APC (562669; clone GHI/61), anti-CD56-APC-R700 (565,139; clone NCAM16.2), and anti-CD8-APC-Cy7 (557834; clone SK1; all from BD Bioscience); and anti-FoxP3-PE (12-4776-42; clone PCH101; from eBioscience).

### Flow cytometry

Cryopreserved single cell suspensions were thawed and stained using the LIVE/DEAD Fixable Aqua Dead Cell Stain Kit (Invitrogen: L34975). The cells were then washed once with 2 ml FACS staining buffer. After centrifugation and removal of the supernatant, the cells were stained with 40  $\mu$ l fluorochrome-conjugated antibody cocktails for 20 min at 4 °C. After one washing step, for the staining of FoxP3, cells were fixed and permeabilized using a FoxP3 staining buffer kit (eBioscience: 00-5523-00) according to the manufacturer's instructions. Multicolor flow cytometry was performed using an LSR II flow cytometer (BD Bioscience), and the data were analyzed by FlowJo V10 software (Treestar).

### Quantification analysis

The number of isolated live single cells from tumor tissues was measured as the cell number/gram of tumor tissue. In

flow cytometric analysis, the percentage of CD45<sup>+</sup> cells among the total singlet cells was first determined. Each immune cell subset was identified by specific lineage markers. The gating strategy for each immune cell subset is presented in Supplementary Figure S1. The percentage of each immune cell subset among the CD45<sup>+</sup> cells was determined, and the number of cells in each immune cell subset was calculated as the cell number/gram of tumor tissue by multiplying the above values.

### Multimodal MRI radiomic features

For all ( $n = 64$ ) patients, multimodal MR images or pre/post-contrast enhanced T1-weighted (T1, T1CE) and T2-weighted fluid attenuated inversion recovery (T2-FLAIR) images as well as relative cerebral blood volume (rCBV) maps obtained from dynamic susceptibility contrast-enhanced (DSC) MRI and apparent diffusion coefficient (ADC) maps obtained from diffusion-weighted images (DWI) were coregistered using NordicICE (NordicNeuroLab, Bergen, Norway). All MRI images were isotropically resampled (1 mm) and skull-stripped using ‘bet’ from the FSL library. Tumor segmentation was performed using a convolutional neural network, the winner of BraTS 2017 [20], followed by manual correction by a neuroradiologist (7 year experience, K.S.C.). Next, pre/postcontrast enhanced T1-weighted and T2-weighted FLAIR images were normalized using the whitestripe [21] R package (R Core Team, Vienna, Austria). For the rCBV and ADC maps, outliers over three times the standard deviation were removed. Finally, a total of 428 features (107 radiomics features for each MRI sequence; 19 first-order, 16 shape-based, 24 Gy level cooccurrence matrix (GLCM), 16 Gy level size zone matrix (GLSZM), 16 Gy level run length matrix (GLRLM), 5 neighboring gray tone difference matrix (NGTDM), and 14 Gy level dependence matrix (GLDM) features) were extracted from the T1CE and T2-FLAIR images and the rCBV, and ADC maps using Pyradiomics [22]. For each T1CE and FLAIR sequence, an enhancing tumor (ET) and a peritumoral edema (ED) subregion mask was used, and a whole mask was used for both the rCBV and ADC maps (detailed in Supplementary Figure S2).

### Development and evaluation of radiomic signatures

For all classifications, sparse partial least squares discriminant analysis (sPLS-DA) was performed to predict the class labels using the mixOmics [23] R package. Because radiomic data is typical high-dimensional data (i.e., dimensionality, or the number of features is larger than the sample size of data), dimension reduction should be performed to avoid both severe multicollinearity of input variables, and overfitting, when developing the prediction model [24].

For example, principal component analysis (PCA) is the most common algorithm for dimension reduction. However, PCA considers only input data (X), maximizing the variance of components. Partial least squares (PLS) is a well-known multivariate projection-based method that maximizes the covariance between components from input (X) and response (Y) variables [24], namely radiomics and immune features in the present study. In other words, PLS is a supervised version of PCA, simultaneously considering input (X) as well as response (Y) variables, instead of considering input (X) variables only. In PLS, a linear combination of variables from each of dataset (X and Y) are called a ‘latent feature’ or ‘latent component’. The weight vectors used to calculate the linear combinations are called the ‘loading’ vectors. Sparse PLS is a variant of PLS, where  $\ell_1$  penalization is applied on the loading vectors associated to the input (X) data, allowing both feature selection for improved interpretability, and computational efficiency [23, 24]. sPLS-DA is a special case of sparse PLS that performs feature selection and multiclass classification in a one-step procedure [24], coding response (Y) variables as dummy block matrix [25]. For sPLS-DA models, hyperparameters such as the number of components and dimension of projection were determined using a grid-search-like manner and cross-validation [23].

We developed four different sPLS-DA models or signatures for predicting immune phenotypes, defined according to 1) T cell fraction (enriched and deficient groups); 2) T cell subclass without Treg (T4<sup>\*</sup> and T8 dominant groups); 3) M2 fraction (M2 high and low groups); and 4) *IDH* genotype (*IDH*-mut and *IDH*-wt groups), using radiomics features, which consist of the significant prognostic factors in the overall survival analysis. For all the signatures, receiver operating characteristic (ROC) analysis was performed to evaluate the performance of the sPLS-DA models using 5-fold cross-validation rather than dividing the data into training and validation sets because of the limited sample size, and reported area under the curve (AUC) scores are mean AUC scores of 5-folds [23, 25]. For feature selection, to evaluate the importance of radiomics features for the prediction of immune phenotypes, the coefficients of variables, or loadings of features, of the first component of radiomics signatures were analyzed. For example, top 10 important features are the radiomic features with 10 largest loadings. For features selection, full dataset was subjected to sPLS-DA in each of the classification models. To visualize the prediction of immune phenotypes by the corresponding radiomics signatures, the results of classification of all subjects, or full dataset, were plotted in the two-dimensional latent space using the first and second components of the signatures as the two axes.

In addition, correlation analysis was performed between the different types of cell counts and the *IDH*-projected

radiomics signature scores obtained from the output of the developed sPLS-DA model to predict *IDH* genotype. The Shapiro–Wilk test was performed for assessing the normality of the distributions of the variables, and Spearman rank correlation analysis was performed when the distribution of variables was not normally distributed.

## Statistics

Descriptive data statistics were visualized using the Tableau Desktop platform (version 2020.1, Tableau Software, Inc., Seattle, WA, USA). Comparative data analysis was conducted using one-way ANOVA with post hoc Tukey honestly significant difference, independent *t* test, and Mann–Whitney U test depending on the number of groups, sample size, and F-distribution. Hierarchical clustering analysis of the raw values of cell number with scaling and centering using Euclidean distance and Ward linkage was performed to identify the T cell-enriched or T cell-deficient groups (Biovinci version 1.1.5, BioTutoring Inc., San Diego, CA, USA). A linear regression model with 95% confidence interval was applied to classify the subgroups of interest. Survival analysis was performed, and cumulative statistics for survival were calculated using the Kaplan–Meier survival analysis and log-rank tests. The significance level was set at  $p < 0.05$ , and statistical analyses were performed using the R free statistical software package (version 3.5.1; <http://www.r-project.org/>).

## Results

### Number of immune cells per unit volume of HGG tissue

A median of 48,050,000 cells (range: 4,600,000–155,000,000) per sample was collected from the core area of HGG tissue weighing from 0.87 to 14.50 g (median 4.92 g). We confirmed that the number of cells, including tumor cells, increased as the volume of tumor tissue increased; however, the unit number of CD45<sup>+</sup> hematopoietic cells was not correlated with either the number of cells in tumor tissue or the tumor tissue volume (Fig. 1a). The median number of CD45<sup>+</sup> cells per gram of HGG core tissue was 865,770, equivalent to 8.0% of the total cells, including tumor cells (Fig. 1b). The absolute numbers of the subclasses of tumor-infiltrating immune cells according to the histological diagnosis are summarized in Table 1. Although the median numbers of tumor-infiltrating immune cells tended to be higher in GBMs than in AAs or AOs, there were no significant differences in every subclass of cells among the histological diagnoses (Fig. 1c, d, e). We were able to ensure that considerable numbers of immune

cells were infiltrated in the core of HGG tissue regardless of histological diagnosis or grade, although they varied among individual patients.

### Prognostic value of quantified distribution of tumor-infiltrating T cells

Hierarchical clustering with a dendrogram revealed a cluster of T cell-enrichment ( $n = 16$ ) and two separate clusters of T cell-deficiency ( $n = 14$ ) (Fig. 2a). There were no statistically significant signatures for histological diagnoses or genomic characteristics that could define the T cell-enriched or T cell-deficient groups (Fig. 2a). However, overall survival was significantly better in the T cell-deficient group than in the T cell-enriched group ( $p = 0.019$ , Fig. 2b). To investigate the effect of quantified tumor-infiltrating T cells on survival prognosis in detail, we sorted the groups with CD4<sup>+</sup> cells dominant over CD8<sup>+</sup> cells ( $n = 13$ , T4 dominant group) and vice versa ( $n = 34$ , T8 dominant group) from the scatter plot of the T cell subclass ratio among CD45<sup>+</sup> cells using a linear regression line with 95% confidential intervals (Fig. 2c). Although there were no biased histological diagnoses between the two groups, the T8 dominant group showed significantly better overall survival than the T4 dominant group ( $p = 0.023$ , Fig. 2d). This prognostic difference was more clearly observed when we performed a similar analysis excluding the regulatory T cell population (Treg, CD4<sup>+</sup>FoxP3<sup>+</sup>CD25<sup>+</sup> cells) from the CD4<sup>+</sup> cells ( $n = 16$ , T4\* dominant group). The overall survival was significantly better in the T8 dominant group than in the T4\* dominant group ( $p = 0.006$ , Fig. 2f). However, the number of Treg cells in HGG tissue was not a pivotal prognostic variable for overall survival. Neither the proportions of CD4<sup>+</sup>FoxP3<sup>+</sup>CD25<sup>+</sup> cells in CD4<sup>+</sup> cells (Supplementary Figure S3A and B) nor the ratio of CD4<sup>+</sup>FoxP3<sup>+</sup>CD25<sup>+</sup> cells versus CD8<sup>+</sup> cells (Supplementary Figure S3C and D) showed any prognostic value for overall survival.

### Tumor-infiltrating macrophage numbers are decreased in *IDH*-mutated gliomas

The numbers of tumor-infiltrating monocytes, including macrophages, were analyzed. Although we could not find any significant differences in the numbers of CD14<sup>+</sup> cells (monocyte/macrophage), CD14<sup>+</sup>CD68<sup>+</sup> cells (tumor-associated macrophage, TAM), and CD14<sup>+</sup>CD68<sup>+</sup>CD163<sup>+</sup> cells (M2-TAM) among the groups of histological diagnoses, there was a significant decrease in the number of TAMs and M2-TAMs in isocitrate dehydrogenase (*IDH*)-mutated gliomas (Fig. 3a, b). We defined the M2-TAM-high group ( $n = 13$ ) by sorting out the higher ratio of M2-TAMs in relation to the ratio of monocytes/macrophages in CD45<sup>+</sup> cells located above the 95% confidence interval of the

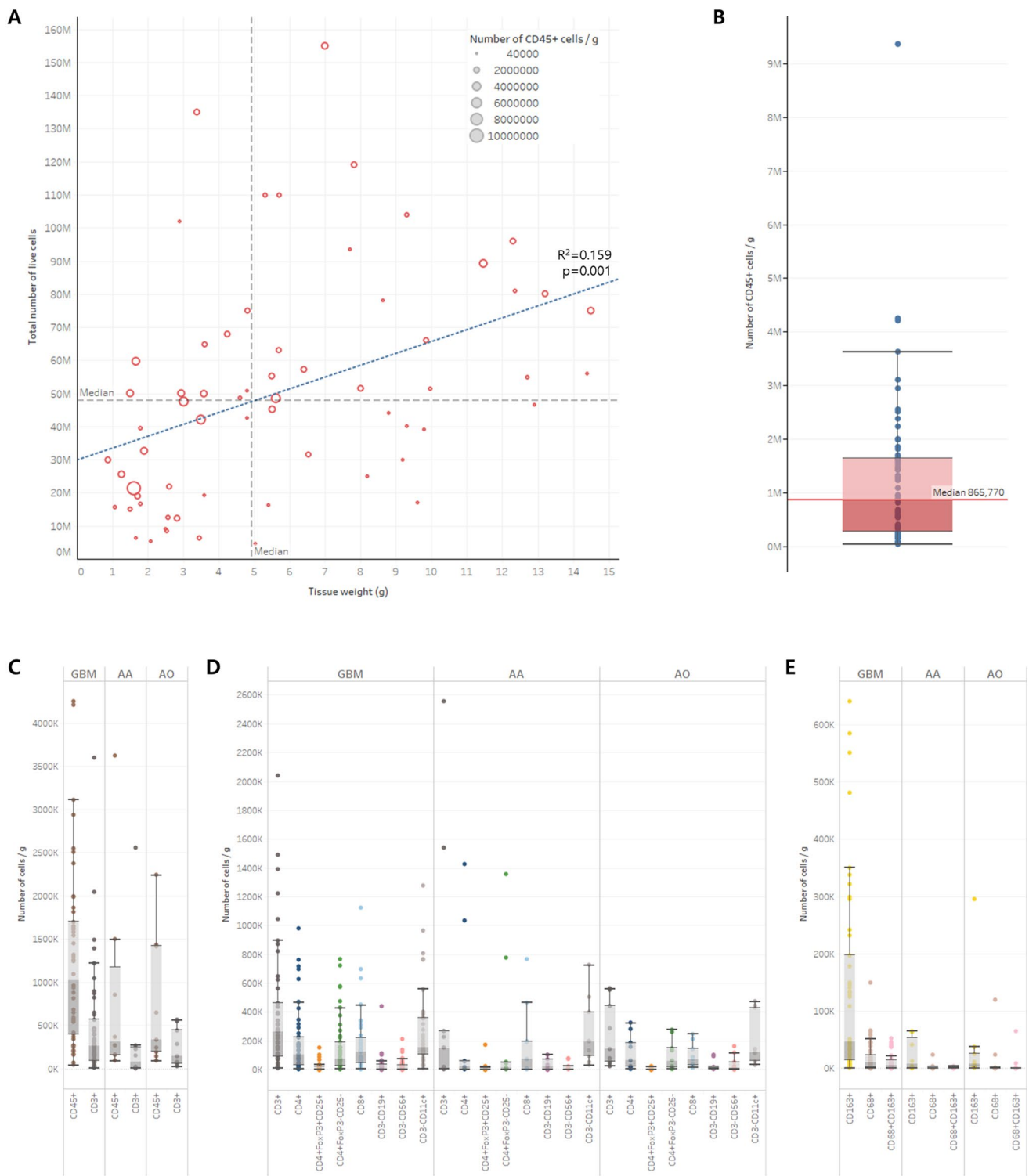


**Fig. 1** Absolute quantification of tumor-infiltrating immune cells in the core area of high-grade gliomas. **a** The total number of live cells is proportional to tumor tissue volume. However, the number of CD45<sup>+</sup> cells (hematopoietic cells) is randomly distributed regardless of the number of cells or tissue volume. **b** The median number of CD45<sup>+</sup> cells was 865,770 per gram of tumor tissue (range: 40,800–

9,362,500). **c** The number of CD45<sup>+</sup> cells and CD3<sup>+</sup> cells (T cells) in glioblastoma (GBM), anaplastic astrocytoma (AA), and anaplastic oligodendroglioma (AO) tissues. **d** The number of CD14<sup>+</sup> immune subclass cells in GBM, AA, and AO tissues. **e** The number of CD14<sup>+</sup> immune subclass cells in GBM, AA, and AO tissues

**Table 1** Number of tumor-infiltrating immune cells per one gram of tumor core tissue

Surface marker	Cell type	GBM		AA		AO	
		Median	95% CI	Median	95% CI	Median	95% CI
CD45 +	Hematopoietic cells	1024,977	101,278	362,000	645,721	335,870	162,195
CD14-CD3 +	T cell	262,696	63,817	151,000	191,113	142,606	47,199
CD4 +	CD4 + T cell	105,000	27,542	19,043	114,850	63,261	26,029
CD4 + FoxP3 + CD25 +	Regulatory CD4 + T cell	8972	2914	1,221	11,973	697	1910
CD4 + FoxP3-CD25-	Non-regulatory CD4 + T cell	87,793	24,368	14,648	102,728	60,600	22,605
CD8 +	CD8 + T cell	126,846	32,655	74,800	56,041	70,767	18,273
CD14-CD3-CD19 +	B cell	9,975	6,595	21,500	9,120	12,700	8,243
CD14-CD3-CD56 +	NK cell	9,485	4,130	6,000	6,524	12,759	12,213
CD14-CD3-CD11c +	Dendritic cell	152,000	26,999	194,000	49,896	118,000	39,564
CD14 +	Monocyte/Macrophage	146,139	34,717	17,578	433,029	26,087	38,406
CD163 +	M2-monocyte/macrophage	46,872	16,592	11,600	364,412	7,510	20,227
CD68 +	TAM	10,296	2642	338	1,625	163	8369
CD68 + CD163 +	M2-TAM	5678	1424	145	342	89	4494

GBM glioblastoma, AA anaplastic astrocytoma, AO anaplastic oligodendroglioma, CI confidence interval, TAM Tumor-associated macrophage

linear regression line, and they were correlated to the number of TAMs (Fig. 3c). The M2-TAM-high group showed a tendency of poorer prognosis than the remaining cases, although the difference in survival was not statistically significant (Fig. 3d,  $p=0.100$ ).

### Radiomics signatures of immune phenotypes

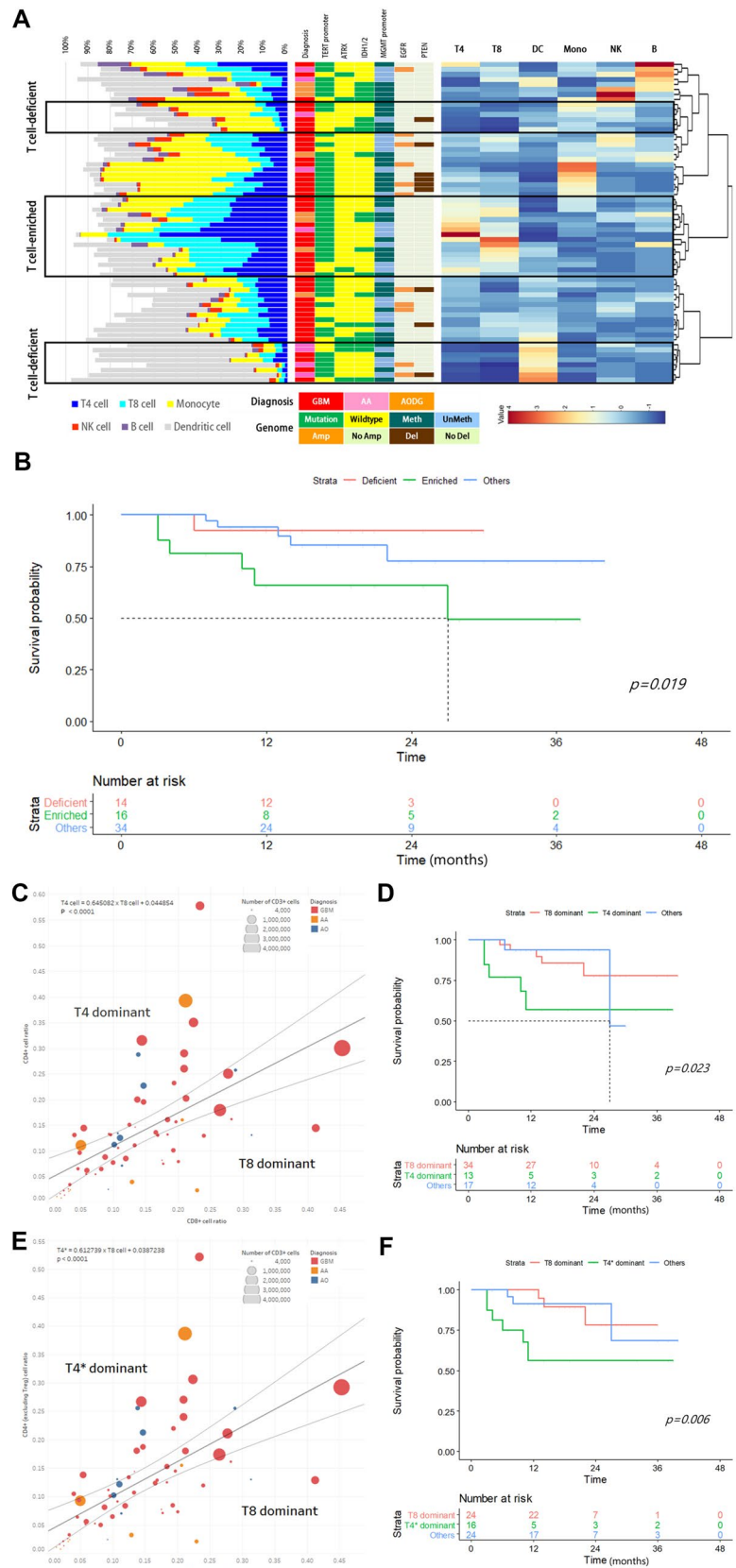
A total of 51 patients were included in the radiomics analysis; 13 patients were excluded for missing rCBV maps ( $n=7$ ) and poor coregistration/segmentation ( $n=6$ ). A heatmap of radiomics features using hierarchical clustering with a dendrogram showed the largest cluster at the left lower corner, which is mostly comprised of GLRLM, GLCM, GLDM, and GLSZM features from T2-FLAIR images and rCBV maps (Fig. 4a). The radiomic signatures of immune phenotypes developed using the sPLS-DA model showed the following diagnostic performance in predicting the immune phenotypes: (1) T cell fraction (enriched and deficient), AUC = 0.986 (95% confidence interval (CI), 0.953–1) ( $p=0.00005$ ); (2) T cell subclass without Treg (T8 and T4\* dominant), AUC = 0.783 (0.643–0.923) ( $p=0.001$ ); (3) M2-TAM fraction (M2-TAM high and low), AUC = 0.798 (0.652–0.944) ( $p=0.003$ ); and (4) *IDH* genotype (*IDH* wt vs mut), AUC = 0.890 (0.801–0.979) ( $p=0.00002$ ). The ROC curves of the four radiomic signatures for immune phenotypes are shown in Fig. 4b. The coefficients of variables of the first component of the radiomics signatures of immune phenotypes are illustrated for all selected features from the sPLS-DA model in the left column of Fig. 4c–f. The immune phenotypes and *IDH* genotype of all subjects were well predicted by the corresponding radiomics signature, as visualized in the right column of Fig. 4c–f.

For T cell fraction prediction, among the top 10 features (5 features from ADC maps, 2 features from rCBV maps, and 3 features from T2-FLAIR images), 5 were GLSZM features, 2 were GLCM features, one was a GLRLM feature, one was an NGTDM feature, and the other was a shape feature. For T cell subclass fraction prediction, among the top 10 features (9 features from T1CE images and 1 feature from ADC maps), 3 were GLRLM features, 3 were GLCM features, 2 were GLDM features, one was a GLSZM feature, and the other was an NGTDM feature. For M2 macrophage fraction prediction, among the top 10 features (8 features from ADC maps, 1 feature from T1CE, and the other one feature from T2-FLAIR images), 4 were first-order features, 2 were GLDM features, 2 were GLCM features, and the other two were shape features. For *IDH* genotype prediction, among the top 10 features (4 features from rCBV maps, 1 feature from ADC maps, and 10 features from T1CE images), 5 features were shape features, 4 features were GLRLM features, and the other feature was a GLDM feature. For each radiomics signature for immune phenotypes and *IDH* genotype, the top 10 selected features of the first component are listed in Table 2.

### Correlation analysis between cell counts and *IDH*-projected radiomic signature scores

Among the different types of cell counts, the *IDH*-projected radiomics signature score was positively correlated with the following: M2-TAM (Spearman's  $\rho=0.458$ ,  $p=0.0008$ ); TAM ( $\rho=0.409$ ,  $p=0.003$ ); M2-monocyte/macrophage ( $\rho=0.326$ ,  $p=0.019$ ); and TIL ( $\rho=0.258$ ,  $p=0.048$ ) (Table 3).

**Fig. 2** Quantification analysis of tumor-infiltrating T cells in high-grade gliomas and their prognostic impact. **a** Hierarchical clustering of the high-grade glioma tissue samples based on the numbers of major immune cell populations. Histological diagnosis and genetic signatures were matched with samples that exhibited no significant preponderance in classified T cell-enriched and T cell-deficient groups. **b** Significant survival differences in T cell-enriched and T cell-deficient groups ( $p=0.019$ ). **c** The ratio of CD4<sup>+</sup> cells (T4 cells) to CD8<sup>+</sup> cells (T8 cells) among CD45<sup>+</sup> cells was plotted, and samples outside the 95% confidence interval of the linear regression line were defined as T4 dominant and T8 dominant groups. **d** The T8 dominant group showed a significant survival advantage over the T4 dominant group ( $p=0.023$ ). **e** The ratio of CD4<sup>+</sup> cells (T4\* cells) excluding CD4<sup>+</sup>FoxP3<sup>+</sup>CD25<sup>+</sup> cells (Treg cells) and CD8<sup>+</sup> cells (T8 cells) among CD45<sup>+</sup> cells were plotted, and samples outside the 95% confidence interval of the linear regression line were defined as T4\* dominant and T8 dominant groups. **f** The T8 dominant group showed a more profoundly significant survival advantage over the T4\* dominant group ( $p=0.006$ )



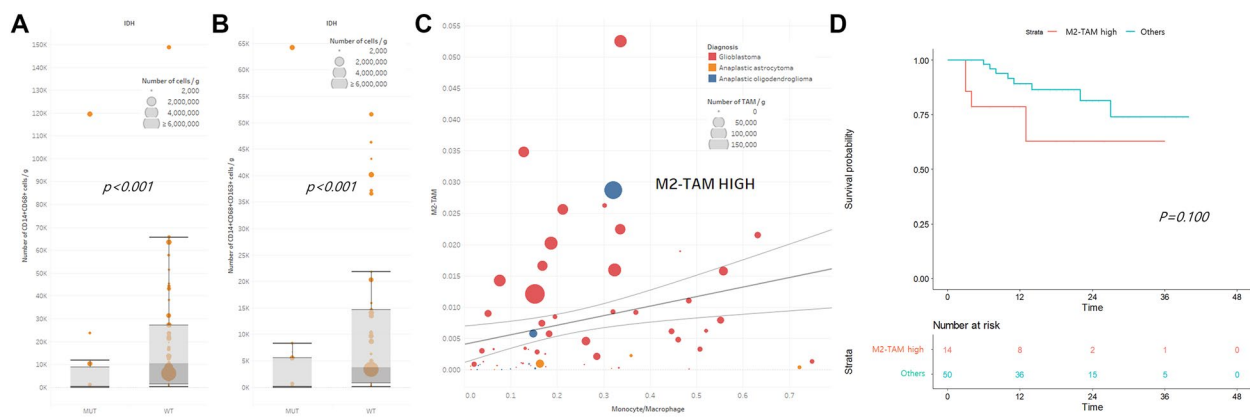


**Fig. 3** Quantification analysis of tumor-infiltrating macrophages in relation to isocitrate dehydrogenase (*IDH*) mutational status in high-grade gliomas. **a** The numbers of CD14<sup>+</sup>CD68<sup>+</sup> cells (tissue macrophages) were significantly decreased in *IDH*-mutant gliomas (median: 519 cells/g, range: 0–11,832) compared with those of *IDH* wild-type gliomas (median: 10,393 cells/g, range: 72–65,690,  $p < 0.001$ ). **b** The numbers of CD14<sup>+</sup>CD68<sup>+</sup> CD163<sup>+</sup> cells (M2 macrophages) were significantly decreased in *IDH*-mutant gliomas

(median: 219 cells/g, range: 0–8276) compared with those of *IDH* wild-type gliomas (median: 3,770 cells/g, range: 80–21,854,  $p < 0.001$ ). **c** The ratio of CD14<sup>+</sup>CD68<sup>+</sup> CD163<sup>+</sup> cells (M2 macrophages) and CD14<sup>+</sup> cells (monocytes) among CD45<sup>+</sup> cells were plotted, and samples above the 95% confidence interval of the linear regression line were defined as the M2 macrophage-high group. **d** Overall survival of the M2 macrophage-high group and of the remaining patients

## Discussion

The International Immuno-oncology Biomarkers Working Group (IBWG) recently proposed standardized methodology guidelines to assess tumor-infiltrating lymphocytes (TILs) in various solid tumors [26]. However, no standardized assessment algorithms for TIL could be proposed for gliomas due to their specific architecture and histomorphology [26]. In the present study, we performed flow cytometric analysis with lineage markers for the identification of various immune cell subsets infiltrating tumor tissues. Flow cytometric analysis is a gold standard method in the identification and phenotyping of immune cell subsets in general. In the current study, based on the weight of tumor tissues and the numbers of dissociated single cells from tumor tissues, we calculated the absolute cell numbers of specific immune subsets, which were defined by flow cytometric analysis per gram of tumor tissues. By this approach, we found that there was a significant correlation between CD8<sup>+</sup> T cell counts and overall patient survival, implying that this methodologic approach is reliable for calculating the absolute cell numbers of specific immune subsets and associating them with clinical outcome.

We found that immune infiltrates are heterogeneous between tumor types and among patients. However, we were able to categorize patients by immune phenotype and correlate these phenotypes with clinical outcome. The density of infiltrating lymphocytes has been reported to be associated with clinical outcome in many different tumor types, although the density was determined by immunohistochemistry, not by flow cytometric analysis [27]. In the case of

HGG, a high density of CD8 + T cells has been reported to correlate with better overall survival [28, 29]. In contrast, the infiltration of CD4 + FoxP3 + CD25 + cells correlates with decreased survival [30]. In the current study, even though overall survival was significantly better in the T cell-deficient group than in the T cell-enriched group, the T8 dominant group showed better overall survival than the T4 and T4\* dominant groups. This result indicates that tumor-infiltrating CD8 + T cells have a significant role in antitumor immunity and that the prognostic value increases when considered with CD4 + FoxP3 + CD25 + cells in the HGG microenvironment.

TAMs are regarded as a macrophage subset differentiated specifically in the tumor microenvironment [31]. In brain tumors, TAMs are abundant and accumulate more with higher tumor grade [32, 33]. Functionally, TAMs in brain tumor microenvironments produce high levels of immunosuppressive cytokines, such as arginase, IL-10, and transforming growth factor- $\beta$ , and downregulate T-cell responses, showing that they are protumorigenic [6]. In glioma tissues, the cells producing IL-10 have been directly implicated as CD68-expressing monocytes and positive for M2 markers CD163 and CD204 [34]. In the current study, we analyzed M2-TAMs as well as TAMs using CD68 and CD163 markers. We found that M2-TAMs were significantly decreased in *IDH*-mutated glioma and tended to be associated with a poor prognosis of HGG patients. Even though relations among the density of M2-TAMs, *IDH* mutation status, and patient prognosis have been previously reported [35], we could suggest a reliable link between the cellular, genetic, and clinical implications in our study by analyzing a large



**Fig. 4** **a** Heatmap of radiomics features using hierarchical clustering with a dendrogram: rows indicate subjects ( $n=51$ ), and columns indicate multimodal radiomics features ( $d=428$ ). **b** Receiver operating characteristic (ROC) curves of radiomics signatures for immune phenotypes: T cell fraction (enriched vs deficient group) (*red*), area under the curve (AUC)=0.986 (95% confidence interval (CI), 0.953–1) ( $p=0.00005$ ); T cell subclass fraction (T8 vs T4\* dominant group) (*green*), AUC=0.783 (0.643–0.923) ( $p=0.001$ ); M2 macrophage fraction (M2 high vs low group), AUC=0.798 (0.652–0.944) ( $p=0.003$ ) (*blue*); and *IDH* genotype (*IDH* wt vs mut group), AUC=0.890 (0.801–0.979) ( $p=0.00002$ ) (*orange*). **c–f**. Coefficients of variables of the first component of the radiomics signatures (*left column*) and prediction results for immune phenotypes (*right column*) of the T cell fraction (**c**), T cell subclass fraction (**d**), M2-TAM fraction (**e**), and *IDH* genotype (**f**). In the left column, the horizontal axis indicates the coefficients of the variables, and the vertical axis indicates the name of the variables. In the right column, the horizontal and vertical axes indicate the first and second components of the radiomics signatures, respectively. Note that crosses (+) and surrounding ellipses indicate the centers of the group of subjects. *ROC* receiver operating characteristic, *AUC* area under the curve, *expl. var.* explained variance of each component, *TAM* tumor-associated macrophage

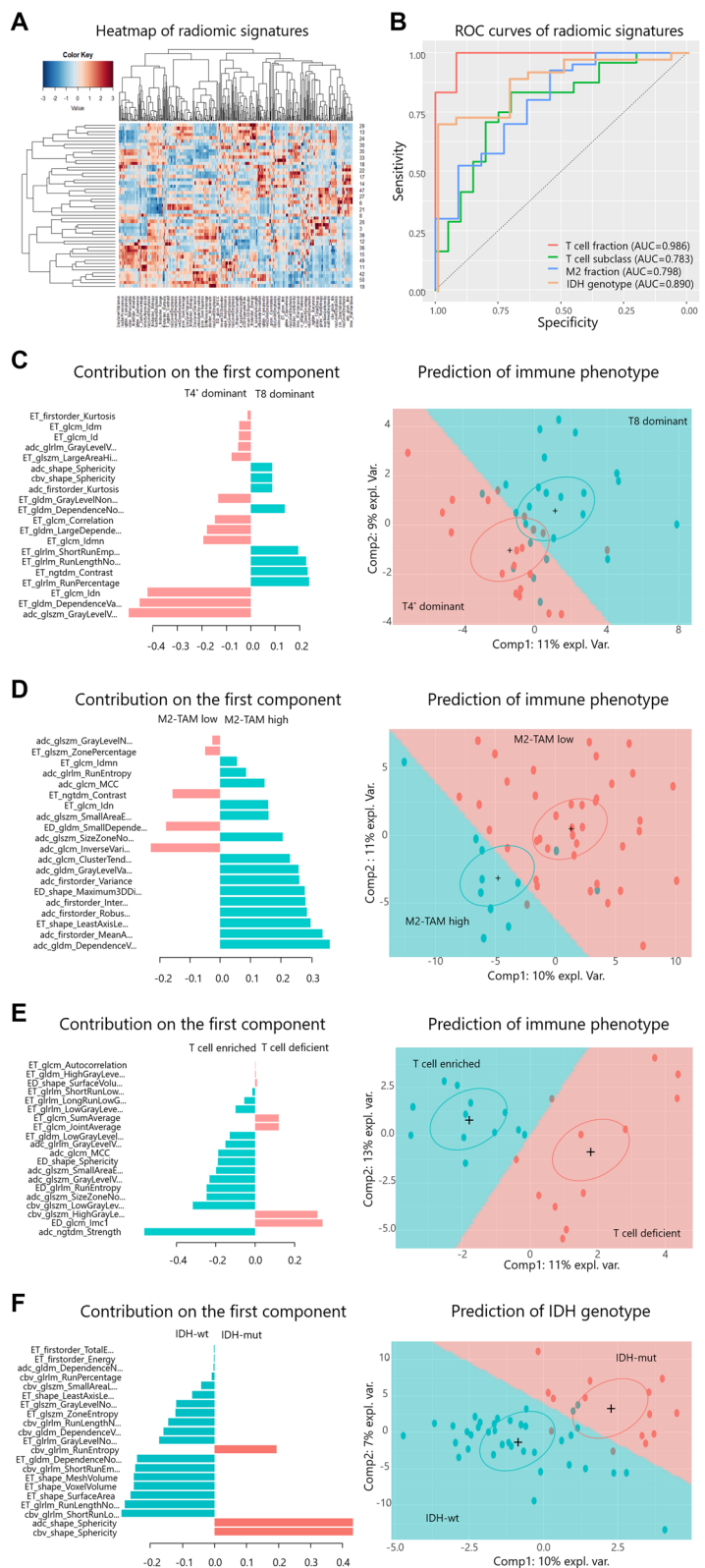


**Table 2** Top 10 selected features of first component of radiomic signatures for immune phenotypes and *IDH* genotype

Immune phenotype	Features with top 10 coefficients <sup>a</sup>	Coefficients	<i>p</i> value <sup>†</sup>
T cell fraction (enriched vs deficient group)	adc_ngtdm_Strength	− 0.563	0.0012*
	ED_glcm_Imc1	0.341	0.0068*
	cbv_glszm_HighGrayLevelZoneEmphasis	0.316	0.0056*
	cbv_glszm_LowGrayLevelZoneEmphasis	− 0.316	0.0001*
	adc_glszm_SizeZoneNonUniformityNormalized	− 0.247	0.0053*
	ED_glrIm_RunEntropy	− 0.246	0.9999
	adc_glszm_GrayLevelVariance	− 0.232	0.9999
	adc_glszm_SmallAreaEmphasis	− 0.197	0.9999
	ED_shape_Sphericity	− 0.189	0.9999
	adc_glcm_MCC	− 0.187	0.9999
T cell subclass fraction (T8 vs T4* dominant group)	adc_glszm_GrayLevelVariance	− 0.499	0.0041*
	ET_gldm_DependenceVariance	− 0.456	0.033*
	ET_glcm_Idn	− 0.422	0.22
	ET_glrIm_RunPercentage	0.239	0.032*
	ET_ngtdm_Contrast	0.233	0.89
	ET_glrIm_RunLengthNonUniformityNormalized	0.227	0.043*
	ET_glrIm_ShortRunEmphasis	0.194	0.50
	ET_glcm_Idmn	− 0.194	0.048*
	ET_gldm_LargeDependenceEmphasis	− 0.179	0.52
	ET_glcm_Correlation	− 0.147	0.44
M2-TAM fraction (M2-TAM high vs low group)	adc_gldm_DependenceVariance	0.362	0.017*
	adc_firstorder_MeanAbsoluteDeviation	0.338	0.40
	ET_shape_LeastAxisLength	0.299	0.09
	adc_firstorder_RobustMeanAbsoluteDeviation	0.286	0.64
	adc_firstorder_InterquartileRange	0.282	0.25
	ED_shape_Maximum3DDiameter	0.280	0.033*
	adc_firstorder_Variance	0.261	0.079
	adc_gldm_GrayLevelVariance	0.260	0.64
	adc_glcm_ClusterTendency	0.230	0.81
	adc_glcm_InverseVariance	− 0.230	0.46
<i>IDH</i> genotype ( <i>IDH</i> mut vs wt group)	cbv_shape_Sphericity	0.595	0.044*
	adc_shape_Sphericity	0.595	0.32
	cbv_glrIm_ShortRunLowGrayLevelEmphasis	− 0.268	0.69
	ET_glrIm_RunLengthNonUniformity	− 0.243	0.21
	ET_shape_SurfaceArea	− 0.203	0.06
	ET_shape_VoxelVolume	− 0.181	0.01*
	ET_shape_MeshVolume	− 0.179	0.10
	cbv_glrIm_ShortRunEmphasis	− 0.167	0.50
	ET_gldm_DependenceNonUniformity	− 0.158	0.09
	cbv_glrIm_RunEntropy	0.047	0.049*

*ET* features from T1-weighted contrast-enhanced images, *ED* features from T2-FLAIR, *adc* features from ADC maps, *cbv* features from rCBV maps, *ndtdm* neighbouring gray tone difference matrix, *glcm* gray level co-occurrence matrix, *gldm* gray level dependence matrix, *glszm* gray level size zone matrix, *glrlm* gray level run length matrix, *shape* shape features, *TAM* tumor-associated macrophage

<sup>†</sup>*p* values of coefficients were given for information purpose only, and should be interpreted with caution, because they were computed using bootstrapping, which leads to unreliable estimation compared to the case of low-dimensional linear regression

<sup>a</sup>Selected features are listed in descending order of absolute values of coefficients of the first component of radiomic signatures

\*Indicates statistical significance (*p* < 0.05)

**Table 3** Correlation between *IDH*-projected radiomic signature scores and immune cell counts

Cell type	Rho <sup>a</sup>	<i>p</i> value
M2-TAM	0.458	0.0008*
TAM	0.409	0.003*
Regulatory T4 cell	0.336	0.016*
Nonregulatory T4 cell	0.328	0.019*
M2-monocyte/macrophage	0.326	0.019*
CD4 + T cell	0.323	0.021*
Monocyte/macrophage	0.301	0.032*
TIL	0.258	0.048*
CD8 + T cell	0.234	0.098
NK cell	0.036	0.80

<sup>a</sup>Spearman's rank correlation rho: listed in descending order of rho values

\*Indicates statistical significance ( $p < 0.05$ )

*IDH* isocitrate dehydrogenase, *TIL* tumor infiltrating lymphocytes, *TAM* tumor-associated macrophage, *NK* natural killer

sample size. More specifically, the *IDH*-predicted radiomics signature score showed a significant correlation with M2-TAM cell counts ( $\rho = 0.45$ ,  $p = 0.0008$ ) in the current study. However, a direct relation needs to be demonstrated for a precise prognostic evaluation and therapeutic approach.

We developed and evaluated radiomics signatures of immune phenotypes using sPLS-DA, showing good diagnostic performance in this study. The result of the present study reproduced that of the study by Sun et al. [36], however, with 'real' cell counts of immune cells, not the 'assumed' immune phenotype using estimated cell counts. Moreover, we analyzed not only CD8+ cells but also 13 distinct types of immune cells. Regardless of immune phenotype, the majority of the top 10 features were from ADC maps, which are important for predicting the immune phenotypes: specifically, T cell fraction (enriched vs deficient group), T cell subclass fraction (T8 vs T4\* dominant group), and M2-TAM fraction (M2-TAM high vs low group). Considering that ADC values represent cellularity and that there should be differences in cellularity between the two groups for each immune phenotype, we can carefully interpret this result as indicating that ADC maps might reflect the tumor immune environment, considering that the tumor cell density would also account for low ADC values to a similar degree, which warrants further investigation. For radiomics signatures built to predict the *IDH* genotype, sphericity [37, 38] and volume [17] features have been reported to be relevant features, which are also shown to be two of the significant features in our results: sphericity and voxel volume from shape features (Table 2). Surprisingly, this result is consistent with the conventional MRI findings of *IDH*-mut tumors: *IDH*-mut astrocytomas tend to have well-defined margins and be less infiltrative with reduced enhancement due to their lower

invasiveness *IDH*-wt astrocytomas [18], which is explained by the positive coefficient of sphericity (0.595), meaning that increased sphericity contributes to the prediction of *IDH*-mut, and by the negative coefficient ( $-0.181$ ) of the voxel volume of the enhancing tumor, meaning that an increased voxel volume of an enhancing tumor contributes to the prediction of *IDH*-wt (Table 2).

Meanwhile, the good diagnostic performance of the developed radiomics signatures of immune phenotypes seem to be correlated with *IDH* status. The *IDH* genotype leads to a distinguished tumor microenvironment including distinctive cytokines, resulting in different immune phenotypes [12]. Furthermore, the *IDH* genotype has recently been shown to be correlated to radiologic phenotypes [39] and thus can be predicted using radiomics or features obtained from multimodal MRI, including perfusion MRI [17, 18]. Therefore, some radiomic features correlated with *IDH* status would also be correlated to specific immune phenotypes, which can explain the good diagnostic performance of the developed radiomics signatures. For example, M2-TAM count was correlated with *IDH*-projected radiomics signature scores. Despite the useful diagnostic impact of radiomics in our studies, the inherent limitation of radiomics methodology need to be considered.

## Conclusion

By acquiring data on the absolute number of immune cells infiltrated in tumor tissue, we aspired to understand the immune microenvironment of HGG more precisely. We also confirmed that the immune microenvironment of HGG is heterogeneous among patients and that certain immune phenotypes are related to prognosis. For better clinical implications, we can predict the immune phenotypes noninvasively using tumor radiomics signatures. A comprehensive understanding of the relationship between the immune microenvironment and the clinical impact and radiomics signatures of HGG is expected to help not only predict prognosis but also apply immune-related treatments in the future.

**Acknowledgements** We thank Hye Jung Hong, R.N. for her support in collecting clinical data and laboratory management in contribution to this study.

**Author contributions** ARK, KSC, MSK, SHC, E-CS and C-K.P wrote the manuscript. C.-KP, E-CS and SHC contributed to the conception and design of the project and revised the manuscript. SK, TC, HJY, and CEL collected tissue samples and performed the experiments. ARK and E-CS performed flow cytometric analysis. KSC and SHC performed the radiomics analysis. K-MK, HK, JHL, S-TL, JWK, Y-HK, and TMK contributed to the collection and analysis of clinical data. JKW and S-HP. performed histological diagnosis and molecular/genetic examinations. All authors participated in drafting and revising

the article for important intellectual content and approved the final version for publication.

**Funding** This work was supported by the following funding sources: a National Research Foundation of Korea (NRF) grant funded by the Korea government Ministry of Science and ICT (MSIT) (NRF-2019R1A2C2005144 to C.-K.P.), the Basic Science Research Program through the National Research Foundation of Korea (NRF) funded by the Ministry of Science, ICT & Future Planning (2020R1A2C2008949 to S.H.C.), the Creative-Pioneering Researchers Program through Seoul National University (SNU; to S.H.C.), and the Institute for Basic Science (IBS-R006-A1 to S.H.C.)

**Data availability** All data are published within this paper and within accompanying supporting files (indicated in text) and accessed via weblink on the journal site.

## Compliance with Ethical Standards

**Conflict of interest** The authors declare no conflict of interest.

**Ethical approval** This study involving human tissue and cells was approved by the Ethics Committee of the Seoul National University Hospital (IRB No. H-1902-062-1010).

**Informed consent to participate** All tissue and data were anonymized. This study was performed in accordance with the Declaration of Helsinki.


## References

- Brooks WH, Markesbery WR, Gupta GD, Roszman TL (1978) Relationship of lymphocyte invasion and survival of brain tumor patients. *Ann Neurol* 4(3):219–224. <https://doi.org/10.1002/ana.410040305>
- Louveau A, Smirnov I, Keyes TJ, Eccles JD, Rouhani SJ, Peske JD, Derecki NC, Castle D, Mandell JW, Lee KS, Harris TH, Kipnis J (2015) Structural and functional features of central nervous system lymphatic vessels. *Nature* 523(7560):337–341. <https://doi.org/10.1038/nature14432>
- Hu X, Deng Q, Ma L, Li Q, Chen Y, Liao Y, Zhou F, Zhang C, Shao L, Feng J, He T, Ning W, Kong Y, Huo Y, He A, Liu B, Zhang J, Adams R, He Y, Tang F, Bian X, Luo J (2020) Meningeal lymphatic vessels regulate brain tumor drainage and immunity. *Cell Res* 30(3):229–243. <https://doi.org/10.1038/s41422-020-0287-8>
- Orrego E, Castaneda CA, Castillo M, Bernabe LA, Casavilca S, Chakravarti A, Meng W, Garcia-Corrochano P, Villa-Robles MR, Zevallos R, Mejia O, Deza P, Belmar-Lopez C, Ojeda L (2018) Distribution of tumor-infiltrating immune cells in glioblastoma. *CNS oncol* 7(4):CNS21. <https://doi.org/10.2217/cns-2017-0037>
- Han S, Zhang C, Li Q, Dong J, Liu Y, Huang Y, Jiang T, Wu A (2014) Tumour-infiltrating CD4(+) and CD8(+) lymphocytes as predictors of clinical outcome in glioma. *Br J Cancer* 110(10):2560–2568. <https://doi.org/10.1038/bjc.2014.162>
- Hussain SF, Yang D, Suki D, Aldape K, Grimm E, Heimberger AB (2006) The role of human glioma-infiltrating microglia/macrophages in mediating antitumor immune responses. *Neuro Oncol* 8(3):261–279. <https://doi.org/10.1215/15228517-2006-008>
- Palma L, Di Lorenzo N, Guidetti B (1978) Lymphocytic infiltrates in primary glioblastomas and recidivous gliomas. Incidence, fate, and relevance to prognosis in 228 operated cases. *J Neurosurg* 49(6):854–861. <https://doi.org/10.3171/jns.1978.49.6.0854>
- Quail DF, Joyce JA (2017) The microenvironmental landscape of brain tumors. *Cancer Cell* 31(3):326–341. <https://doi.org/10.1016/j.ccell.2017.02.009>
- Liu Z, Meng Q, Bartek J Jr, Poiret T, Persson O, Rane L, Rangulova E, Illies C, Peredo IH, Luo X, Rao MV, Robertson RA, Dodoo E, Maeurer M (2017) Tumor-infiltrating lymphocytes (TILs) from patients with glioma. *Oncoimmunology* 6(2):e1252894. <https://doi.org/10.1080/2162402X.2016.1252894>
- Gabusiewicz K, Rodriguez B, Wei J, Hashimoto Y, Healy LM, Maiti SN, Thomas G, Zhou S, Wang Q, Elakkad A, Liebelt BD, Yaghi NK, Ezhilarasan R, Huang N, Weinberg JS, Prabhu SS, Rao G, Sawaya R, Langford LA, Bruner JM, Fuller GN, Bar-Or A, Li W, Colen RR, Curran MA, Bhat KP, Antel JP, Cooper LJ, Sulman EP, Heimberger AB (2016) Glioblastoma-infiltrated innate immune cells resemble M0 macrophage phenotype. *JCI Insight*. <https://doi.org/10.1172/jci.insight.85841>
- Brandenburg S, Turkowski K, Mueller A, Radev YT, Seidlitz S, Vajkoczy P (2017) Myeloid cells expressing high level of CD45 are associated with a distinct activated phenotype in glioma. *Immunol Res* 65(3):757–768. <https://doi.org/10.1007/s12026-017-8915-1>
- Berghoff AS, Kiesel B, Widhalm G, Wilhelm D, Rajky O, Kurscheid S, Kresl P, Wohrer A, Marosi C, Hegi ME, Preusser M (2017) Correlation of immune phenotype with IDH mutation in diffuse glioma. *Neuro Oncol* 19(11):1460–1468. <https://doi.org/10.1093/neuonc/nox054>
- Yu P, Fu YX (2006) Tumor-infiltrating T lymphocytes: friends or foes? *Laboratory Invest* 86(3):231–245. <https://doi.org/10.1038/labinvest.3700389>
- Zhang J, Caruso FP, Sa JK, Justesen S, Nam DH, Sims P, Caccarelli M, Lasorella A, Iavarone A (2019) The combination of neoantigen quality and T lymphocyte infiltrates identifies glioblastomas with the longest survival. *Commun Biol* 2:135. <https://doi.org/10.1038/s42003-019-0369-7>
- Castaneda CA, Castillo M, Aliaga K, Bernabe LA, Casavilca S, Sanchez J, Torres-Cabala CA, Gomez HL, Mas L, Dunstan J, Cotrina JM, Abugattas J, Chavez I, Ruiz E, Montenegro P, Rojas V, Orrego E, Galvez-Nino M, Felix B, Landa-Baella MP, Vidaurre T, Villa MR, Zevallos R, Taxa L, Guerra H (2019) Level of tumor-infiltrating lymphocytes and density of infiltrating immune cells in different malignancies. *Biomark Med* 13(17):1481–1491. <https://doi.org/10.2217/bmm-2019-0178>
- Martinez-Lage M, Lynch TM, Bi Y, Cocito C, Way GP, Pal S, Haller J, Yan RE, Ziober A, Nguyen A, Kandpal M, O'Rourke DM, Greenfield JP, Greene CS, Davuluri RV, Dahmane N (2019) Immune landscapes associated with different glioblastoma molecular subtypes. *Acta Neuropathol Commun* 7(1):203. <https://doi.org/10.1186/s40478-019-0803-6>
- Zhang B, Chang K, Ramkissoon S, Tanguturi S, Bi WL, Reardon DA, Ligon KL, Alexander BM, Wen PY, Huang RY (2017) Multimodal MRI features predict isocitrate dehydrogenase genotype in high-grade gliomas. *Neuro Oncol* 19(1):109–117
- Choi KS, Choi SH, Jeong B (2019) Prediction of IDH genotype in gliomas with dynamic susceptibility contrast perfusion MR imaging using an explainable recurrent neural network. *Neuro Oncol* 21(9):1197–1209
- Binnewies M, Roberts EW, Kersten K, Chan V, Fearon DF, Merad M, Coussens LM, Gabrilovich DI, Ostrand-Rosenberg S, Hedrick CC (2018) Understanding the tumor immune microenvironment (TIME) for effective therapy. *Nat Med* 24(5):541–550
- Wang G, Li W, Vercauteren T, Ourselin S (2019) Automatic brain tumor segmentation based on cascaded convolutional neural networks with uncertainty estimation. *Front Comput Neurosci* 13:56

21. Shinohara RT, Sweeney EM, Goldsmith J, Shiee N, Mateen FJ, Calabresi PA, Jarso S, Pham DL, Reich DS, Crainiceanu CM (2014) Statistical normalization techniques for magnetic resonance imaging. *NeuroImage Clin* 6:9–19
22. Van Griethuysen JJ, Fedorov A, Parmar C, Hosny A, Aucoin N, Narayan V, Beets-Tan RG, Fillion-Robin J-C, Pieper S, Aerts HJ (2017) Computational radiomics system to decode the radiographic phenotype. *Can Res* 77(21):e104–e107
23. Rohart F, Gautier B, Singh A, Lê Cao K-A (2017) mixOmics: an R package for ‘omics feature selection and multiple data integration. *PLoS Comput Biol* 13(11):e1005752
24. Le Cao KA, Boitard S, Besse P (2011) Sparse PLS discriminant analysis: biologically relevant feature selection and graphical displays for multiclass problems. *BMC Bioinformatics* 12:253. <https://doi.org/10.1186/1471-2105-12-253>
25. Barker M, Rayens W (2003) Partial least squares for discrimination. *J Chemom* 17(3):166–173
26. Hendry S, Salgado R, Gevaert T, Russell PA, John T, Thapa B, Christie M, van de Vijver K, Estrada MV, Gonzalez-Ericsson PI, Sanders M, Solomon B, Solinas C, Van den Eynden G, Allory Y, Preusser M, Hainfellner J, Pruneri G, Vingiani A, Demaria S, Symmans F, Nuciforo P, Comerma L, Thompson EA, Lakhani S, Kim SR, Schnitt S, Colpaert C, Sotiriou C, Scherer SJ, Ignatiadis M, Badve S, Pierce RH, Viale G, Sirtaine N, Penault-Llorca F, Sugie T, Fineberg S, Paik S, Srinivasan A, Richardson A, Wang Y, Chmielik E, Brock J, Johnson DB, Balko J, Wienert S, Bossuyt V, Michiels S, Ternes N, Burchardi N, Luen SJ, Savas P, Klauschen F, Watson PH, Nelson BH, Criscitiello C, O’Toole S, Larsimont D, de Wind R, Curigliano G, Andre F, Lacroix-Triki M, van de Vijver M, Rojo F, Floris G, Bedri S, Sparano J, Rimm D, Nielsen T, Kos Z, Hewitt S, Singh B, Farshid G, Loibl S, Allison KH, Tung N, Adams S, Willard-Gallo K, Horlings HM, Gandhi L, Moreira A, Hirsch F, Dieci MV, Urbanowicz M, Brcic I, Korski K, Gaire F, Koeppen H, Lo A, Giltnane J, Rebelatto MC, Steele KE, Zha J, Emancipator K, Juco JW, Denkert C, Reis-Filho J, Loi S, Fox SB (2017) Assessing tumor-infiltrating lymphocytes in solid tumors: a practical review for pathologists and proposal for a standardized method from the international immuno-oncology biomarkers working group: part 2: TILs in melanoma, gastrointestinal tract carcinomas, non-small cell lung carcinoma and mesothelioma, endometrial and ovarian carcinomas, squamous cell carcinoma of the head and neck, genitourinary carcinomas, and primary brain tumors. *Adv Anat Pathol* 24(6):311–335. <https://doi.org/10.1097/PAP.0000000000000161>
27. Fridman WH, Pages F, Sautes-Fridman C, Galon J (2012) The immune contexture in human tumours: impact on clinical outcome. *Nat Rev Cancer* 12(4):298–306. <https://doi.org/10.1038/nrc3245>
28. Kim YH, Jung TY, Jung S, Jang WY, Moon KS, Kim IY, Lee MC, Lee JJ (2012) Tumour-infiltrating T-cell subpopulations in glioblastomas. *Br J Neurosurg* 26(1):21–27. <https://doi.org/10.3109/02688697.2011.584986>
29. Yang I, Tihan T, Han SJ, Wrensch MR, Wiencke J, Sughrue ME, Parsa AT (2010) CD8+ T-cell infiltrate in newly diagnosed glioblastoma is associated with long-term survival. *J Clin Neurosci* 17(11):1381–1385. <https://doi.org/10.1016/j.jocn.2010.03.031>
30. Yue Q, Zhang X, Ye HX, Wang Y, Du ZG, Yao Y, Mao Y (2014) The prognostic value of Foxp3+ tumor-infiltrating lymphocytes in patients with glioblastoma. *J Neurooncol* 116(2):251–259. <https://doi.org/10.1007/s11060-013-1314-0>
31. Franklin RA, Liao W, Sarkar A, Kim MV, Bivona MR, Liu K, Pamer EG, Li MO (2014) The cellular and molecular origin of tumor-associated macrophages. *Science* 344(6186):921–925. <https://doi.org/10.1126/science.1252510>
32. Hambardzumyan D, Gutmann DH, Kettenmann H (2016) The role of microglia and macrophages in glioma maintenance and progression. *Nat Neurosci* 19(1):20–27. <https://doi.org/10.1038/nn.4185>
33. Tomaszewski W, Sanchez-Perez L, Gajewski TF, Sampson JH (2019) Brain tumor microenvironment and host state: implications for immunotherapy. *Clin Cancer Res* 25(14):4202–4210. <https://doi.org/10.1158/1078-0432.CCR-18-1627>
34. Prosniak M, Harshyne LA, Andrews DW, Kenyon LC, Bedelbaeva K, Apanasovich TV, Heber-Katz E, Curtis MT, Cotzia P, Hooper DC (2013) Glioma grade is associated with the accumulation and activity of cells bearing M2 monocyte markers. *Clin Cancer Res* 19(14):3776–3786. <https://doi.org/10.1158/1078-0432.CCR-12-1940>
35. Poon CC, Gordon PMK, Liu K, Yang R, Sarkar S, Mirzaei R, Ahmad ST, Hughes ML, Yong VW, Kelly JJP (2019) Differential microglia and macrophage profiles in human IDH-mutant and -wild type glioblastoma. *Oncotarget* 10(33):3129–3143. <https://doi.org/10.18632/oncotarget.26863>
36. Sun R, Limkin EJ, Vakalopoulou M, Dercle L, Champiat S, Han SR, Verlingue L, Brandao D, Lancia A, Ammari S (2018) A radiomics approach to assess tumour-infiltrating CD8 cells and response to anti-PD-1 or anti-PD-L1 immunotherapy: an imaging biomarker, retrospective multicohort study. *Lancet Oncol* 19(9):1180–1191
37. Choi Y, Nam Y, Lee YS, Kim J, Ahn K-J, Jang J, Shin N-Y, Kim B-S, Jeon S-S (2020) IDH1 mutation prediction using MR-based radiomics in glioblastoma: comparison between manual and fully automated deep learning-based approach of tumor segmentation. *Eur J Radiol*. <https://doi.org/10.1016/j.ejrad.2020.109031>
38. Yu J, Shi Z, Lian Y, Li Z, Liu T, Gao Y, Wang Y, Chen L, Mao Y (2017) Noninvasive IDH1 mutation estimation based on a quantitative radiomics approach for grade II glioma. *Eur Radiol* 27(8):3509–3522
39. Patel SH, Poisson LM, Brat DJ, Zhou Y, Cooper L, Snuderl M, Thomas C, Franceschi AM, Griffith B, Flanders AE (2017) T2-FLAIR mismatch, an imaging biomarker for IDH and 1p/19q status in lower-grade gliomas: a TCGA/TClA project. *Clin Cancer Res* 23(20):6078–6085

**Publisher’s Note** Springer Nature remains neutral with regard to jurisdictional claims in published maps and institutional affiliations.

## Affiliations

A. Reum Kim<sup>1</sup> · Kyu Sung Choi<sup>1</sup> · Min-Sung Kim<sup>2,3</sup> · Kyung-Min Kim<sup>2,3</sup> · Ho Kang<sup>2,3</sup> · Sojin Kim<sup>2,3</sup> · Tamrin Chowdhury<sup>2,3</sup> · Hyeon Jong Yu<sup>2,3</sup> · Chae Eun Lee<sup>2,3</sup> · Joo Ho Lee<sup>3,4</sup> · Soon-Tae Lee<sup>3,5</sup> · Jae Kyung Won<sup>3,6</sup> · Jin Wook Kim<sup>2,3</sup> · Yong-Hwy Kim<sup>2,3</sup> · Tae Min Kim<sup>3,7</sup> · Sung-Hye Park<sup>3,6</sup> · Seung Hong Choi<sup>3,8</sup> · Eui-Cheol Shin<sup>1</sup> · Chul-Kee Park<sup>2,3</sup> 

- <sup>1</sup> Graduate School of Medical Science and Engineering, Korea Advanced Institute of Science and Technology, KAIST, 291 Daehak-ro, Yuseong-gu, Daejeon 34141, Korea
- <sup>2</sup> Department of Neurosurgery, Seoul National University Hospital, 101 Daehak-ro, Jongno-gu, Seoul 03080, Korea
- <sup>3</sup> Seoul National University College of Medicine, 101 Daehak-ro, Jongno-gu, Seoul 03080, South Korea
- <sup>4</sup> Department of Radiation Oncology, Seoul National University Hospital, 101 Daehak-ro, Jongno-gu, Seoul 03080, Korea
- <sup>5</sup> Department of Neurology, Seoul National University Hospital, 101 Daehak-ro, Jongno-gu, Seoul 03080, Korea
- <sup>6</sup> Department of Pathology, Seoul National University Hospital, 101 Daehak-ro, Jongno-gu, Seoul 03080, Korea
- <sup>7</sup> Department of Internal Medicine, Seoul National University Hospital, 101 Daehak-ro, Jongno-gu, Seoul 03080, Korea
- <sup>8</sup> Department of Radiology, Seoul National University Hospital, 101 Daehak-ro, Jongno-gu, Seoul 03080, Korea